

Terrestrial Matter Effects on Reactor Antineutrino Oscillations: Constant vs. Fluctuated Density Profiles

Yu-Feng Li^{1,5 *}, Andong Wang^{2 †}, Ya Xu^{3 ‡}, Jing-yu Zhu^{4 §}

¹Institute of High Energy Physics, Chinese Academy of Sciences, Beijing 100049, China

²State Key Laboratory of Nuclear Resources and Environment, East China University of Technology, Nanchang, China

³Institute of Geology and Geophysics, Chinese academy of sciences, Beijing 100029, China

⁴Institute of Modern Physics, Chinese Academy of Sciences, Lanzhou, 730000, China

⁵School of Physical Sciences, University of Chinese Academy of Sciences, Beijing 100049, China

Abstract

The JUNO Collaboration has recently released its first reactor antineutrino oscillation result, achieving unprecedented precision in the measurement of Δm_{21}^2 and $\sin^2 \theta_{12}$. We emphasize that the accurate determination and modeling of the terrestrial matter density profile are fundamental for extracting the oscillation parameters and probing the neutrino mass ordering. This paper presents a realistic piecewise-constant model for the shallow crustal density profile along the baselines from Taishan and Yangjiang to the experimental hall, based on geological and petrophysical information. The uncertainty in the density profiles arises from variations in the density and length of each segment, both of which are conservatively estimated to be 10%. A careful comparison of constant and fluctuated density profiles is provided and the implications for the precision measurement of oscillation parameters are discussed. Finally, we also discuss the possibility of tomography of the shallow Earth's crust in future reactor neutrino experiments.

*liyufeng@ihep.ac.cn

†adwang2013@ecut.edu.cn

‡xuya@mail.igcas.ac.cn

§zhujingyu@impcas.ac.cn (corresponding author)

1 Introduction

The discovery of the neutrino oscillation phenomena [1, 2], which demonstrated that neutrinos have masses and that lepton flavors are mixed, marks a significant milestone in particle physics. Over the past two decades, numerous solar, atmospheric, reactor, and accelerator neutrino experiments have collected a substantial number of neutrino events [3] and established a coherent picture of the three-flavor neutrino oscillation framework [4–6], which is described by the 3×3 Pontecorvo–Maki–Nakagawa–Sakata (PMNS) [7–9] matrix:

$$U = \begin{pmatrix} c_{12}c_{13} & s_{12}c_{13} & s_{13}e^{-i\delta} \\ -s_{12}c_{23} - c_{12}s_{13}s_{23}e^{i\delta} & c_{12}c_{23} - s_{12}s_{13}s_{23}e^{i\delta} & c_{13}s_{23} \\ s_{12}s_{23} - c_{12}s_{13}c_{23}e^{i\delta} & -c_{12}s_{23} - s_{12}s_{13}c_{23}e^{i\delta} & c_{13}c_{23} \end{pmatrix}, \quad (1.1)$$

with $c_{ij} \equiv \cos \theta_{ij}$ and $s_{ij} \equiv \sin \theta_{ij}$ ($ij = 12, 13, 23$), and δ the Dirac CP-violating phase, and three mass-squared differences:

$$\Delta m_{ij}^2 = m_i^2 - m_j^2, \quad (1.2)$$

where ($i, j = 1, 2, 3$, $i > j$) and m_i is the mass of the i -th mass eigenstate ν_i .

The three-flavor oscillation framework has been successfully measured and tested to within a few percent [4–6]. However, several key scientific questions remain unanswered. Most notably, the ordering of the neutrino mass spectrum—normal mass ordering (NMO: $m_1 < m_2 < m_3$) versus inverted mass ordering (IMO: $m_3 < m_1 < m_2$)—is still unknown, as is the value of the Dirac CP-violating phase δ . In addition, the absolute neutrino mass scale and the nature of neutrino masses—specifically, whether neutrinos are Dirac or Majorana particles—remain unknown. They can be probed by β decay and neutrinoless double- β -decay experiments, as well as cosmological observations [10–13].

The global neutrino program in the coming decades is organized around these promising frontiers. Next-generation long-baseline accelerator experiments such as Hyper-Kamiokande [14] and DUNE [15] aim to precisely measure the atmospheric oscillation parameters and the CP-violating phase δ . On the reactor side, the Jiangmen Underground Neutrino Observatory (JUNO) [16, 17] is a next-generation oscillation experiments aiming at the determination of neutrino mass ordering [18, 19] and measuring oscillation parameters with sub-percent precision [20]. All of these next-generation neutrino oscillation experiments will operate in an era of high precision and require better control of systematic uncertainties on both the theoretical and experimental sides.

The JUNO experiment, the first of these next-generation flagship experiments to begin operations, has published its initial reactor antineutrino oscillation results [21, 22]. It achieved unprecedented precision in measuring Δm_{21}^2 and $\sin^2 \theta_{12}$, with uncertainties of 1.55% and 2.81%, respectively. With this accuracy level, the corrections due to terrestrial matter effects [23, 24] on Δm_{21}^2 and $\sin^2 \theta_{12}$ will be at the percent level [25, 26], and cannot be neglected in the analysis. In the previous analyses, a constant density profile, characterized by an average crustal density, was assumed and deemed reasonably accurate. However, since the majority of the neutrino propagation trajectories are relatively shallow,

the density variation may be significant depending on the local geological conditions. Therefore, it is important to evaluate the effect of a variable density profile on the survival probability and its potential impact on the oscillation parameters.

In this work, we focus on the impact of realistic crustal density variations along the JUNO baselines. By utilizing geological maps and petrophysical data from South China, we construct a piecewise-constant matter density model for the density profiles extending from the Taishan and Yangjiang nuclear power plants to the experimental hall. We evaluate the uncertainties in the density profiles by incorporating detailed local information regarding crustal density and geometric baseline variations in each segment. Using an efficient semi-analytical method based on the Cayley-Hamilton theorem, we compare the differences in neutrino survival probabilities between the variable density profile and its constant density approximation, and discuss the potential impact on future measurements of oscillation parameters. Finally, we explore the possibility of shallow Earth crust tomography in future reactor neutrino experiments.

The remainder of this paper is organized as follows: In Sec. 2, we construct the density profile model along the Taishan–JUNO and Yangjiang–JUNO baselines using geological information. In Sec. 3, we provide a brief recap of three-flavor neutrino oscillations in matter and introduce the semi-analytical formalism used to analyze piecewise-constant density profiles. Sec. 4 presents our numerical results for the survival probabilities and illustrates the impacts of different choices of density profiles. In Sec. 5, we further investigate the impact of possible anomalous density perturbations, such as localized water- or air-like structures along the baselines, and discuss their implications for shallow crust tomography with reactor antineutrinos. Finally, our conclusions and a brief outlook are provided in Sec. 6.

2 Matter density profile along the baselines

2.1 Geological model and baseline discretizations

The JUNO detector is located about 650 m underground, whereas the reactors are slightly above sea level. Reactor antineutrinos thus propagate predominantly through the upper crust, over relatively shallow depths. In this regime, lateral variations of the density are dominated by changes in outcropping strata and lithology rather than by large-scale crust–mantle structures. Under these conditions, it is reasonable to approximate each surface geological unit by a representative bulk density; residual small-scale variations are expected at the level of a few percent. In the following sections we adopt segment-wise fluctuations up to $\pm 10\%$ as a deliberately conservative bound that comfortably covers these geophysical uncertainties.

We briefly summarize the construction of our density profile model. Figure 1 shows the topographic and geological maps of the JUNO detector site at Jiangmen and the two reactor complexes, Taishan (TS) and Yangjiang (YJ). The topographic map illustrates the surface elevation along the two baselines, while the geological map displays the distribution of surface rock units in South China. The white lines indicate the straight baselines from the reactor cores to JUNO, which traverse a

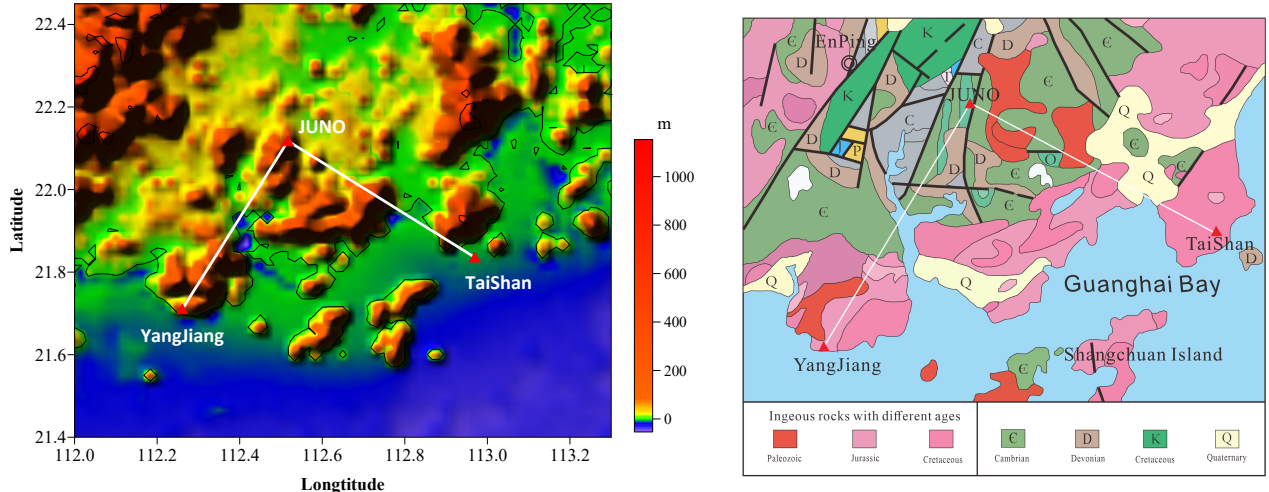


Figure 1: Topographic (left) and geological (right) maps around the JUNO detector site and the Taishan (TS) and Yangjiang (YJ) reactor complexes. The white lines indicate the baselines from the reactor cores to JUNO.

variety of surface geological units. The density structure along each baseline is inferred from these mapped geological units together with the petrophysical properties of the corresponding strata and rock types [27].

To model the matter density along these baselines, we extract the strata and lithology units intersected by the straight line connecting each reactor complex to the JUNO detector from the geological map. Wherever the baseline crosses a boundary between two mapped surface geological units, we define a new segment. In this way, the path from Taishan to JUNO is divided into 12 rock segments, and the path from Yangjiang to JUNO into 14 rock segments. The length of each segment is determined by the distance between consecutive intersections with geological boundaries.

It is worth noting that the actual oscillation baselines are slightly tilted with respect to the local ground surface, since the reactor cores are located about 2 m above ground level, while the JUNO detector is situated at a depth of about 750 m underground. Along the straight line connecting a reactor core to the JUNO detector, the antineutrinos therefore first propagate over a short distance in air before entering the shallow crust. In our piecewise-constant description we account for this by adding an initial segment with density $\rho = 0$ in front of the rock segments listed in Tables 1 and 2. As a result, although the geological sampling along the TS–JUNO (YJ–JUNO) baseline yields 12 (14) rock segments, the effective profiles used in the oscillation calculations consist of $N_{\text{TS}} = 13$ and $N_{\text{YJ}} = 15$ segments in total, including the initial air segment. This segmented representation of the baselines will be used in the following both for the discussion of matter effects and for comparison with previous studies based on a constant-density approximation.

Previous studies have conducted extensive tests and summarized the density characteristics of typical strata and rocks in South China, as compiled in Ref. [27]. The densities assigned to each segment are based on typical rock densities for the corresponding lithology along the JUNO baselines. The resulting segment lengths, densities and rock types for TS–JUNO and YJ–JUNO are summarized

in Tables 1 and 2, respectively. The surface elevation and the associated surface density along each baseline are plotted in Figs. 2 and 3. These figures illustrate that the density variations are relatively modest, typically at the level of a few percent around a mean crustal density of $\sim 2.5 \text{ g/cm}^3$.

2.2 Fluctuations of the matter density profile

In the following we discuss how to model realistic fluctuations of the matter density profile along the Taishan–JUNO and Yangjiang–JUNO baselines, and clarify their impact on the effective average density that enters the neutrino oscillation probabilities.

For definiteness, we denote the reference piecewise-constant profile obtained from the geological information in Sec. 2.1 by $\{\rho_i^{(0)}, L_i^{(0)}\}$, where $\rho_i^{(0)}$ and $L_i^{(0)}$ are the density and length of the i -th segment, and $\sum_i L_i^{(0)} = L$ is the total baseline length. As discussed in Sec. 2.1, the Taishan–JUNO baseline is divided into $N_{\text{TS}} = 13$ segments and the Yangjiang–JUNO baseline into $N_{\text{YJ}} = 15$ segments. The first segment in both cases corresponds to propagation in air, and thus its matter density is set to zero and not allowed to fluctuate.

Distance (km)	Density (g/cm^3)	Rock types
11.5	2.61	Cretaceous: biotite granite
14.8	2.49	Quaternary
20.6	2.49	Quaternary
25.4	2.61	Cretaceous: biotite granite
27.5	2.52	Cambrian: interbedded sandstone–shale or slate, with limestone, sandy gravel, and stone coal
32.6	2.54	Paleozoic: plagioclase-rich granite
39.2	2.52	Cambrian: interbedded sandstone–shale or slate, with limestone, sandy gravel, and stone coal
41.7	2.55	Paleozoic: rhyolite porphyry
46.7	2.53	Cambrian: interbedded sandstone–shale or slate, with limestone, sandy gravel, and stone coal
48.5	2.62	Paleozoic: granodiorite
52.0	2.52	Cambrian: interbedded sandstone–shale or slate, with limestone, sandy gravel, and stone coal
52.7	2.51	Ordovician: graptolite shale, siliceous shale, sandstone, with interbedded conglomerate

Table 1: Matter density sampling and corresponding rock types along the baseline from Taishan (TS) to JUNO. The distances are rounded to one decimal place.

Distance (km)	Density (g/cm ³)	Rock types
11.5	2.60	Jurassic: biotite granite, monzogranite
15.0	2.61	Paleozoic: granite, gneissic granite
16.1	2.55	Jurassic: biotite granite, monzogranite
18.9	2.58	Jurassic: granite porphyry
19.8	2.61	Cretaceous: quartz syenite
26.5	2.52	Cambrian: interbedded sandstone–shale or slate, with limestone, sandy gravel, and stone coal
29.5	2.57	Unmapped area, inferred to be Cambrian or Middle to Upper Devonian
33.3	2.52	Cambrian: interbedded sandstone–shale or slate, with limestone, sandy gravel, and stone coal
35.2	2.57	Devonian
40.7	2.52	Cambrian: interbedded sandstone–shale or slate, with limestone, sandy gravel, and stone coal
43.7	2.51	Ordovician: graptolite shale, siliceous shale, sandstone, with interbedded conglomerate
47.4	2.57	Devonian
48.9	2.52	Cambrian: interbedded sandstone–shale or slate, with limestone, sandy gravel, and stone coal
52.5	2.52	Ordovician: graptolite shale, siliceous shale, sandstone, with interbedded conglomerate

Table 2: Matter density sampling and corresponding rock types along the baseline from Yangjiang (YJ) to JUNO. The distances are rounded to one decimal place.

The baseline-averaged matter density corresponding to the reference profile is defined as

$$\rho^{\text{Average}} = \frac{1}{L} \sum_{i=1}^N \rho_i^{(0)} L_i^{(0)}, \quad (2.3)$$

with $N = N_{\text{TS}} = 13$ or $N = N_{\text{YJ}} = 15$ for the two baselines. Using the segment densities and lengths in Tables 1 and 2 we obtain $\rho_{\text{TS}}^{\text{Average}} \simeq 2.541 \text{ g/cm}^3$ and $\rho_{\text{YJ}}^{\text{Average}} \simeq 2.554 \text{ g/cm}^3$, which will be used as the benchmark input of the constant-density approximation in Sec. 4.

In the numerical calculations of Sec. 4, this piecewise-constant profile is used as the reference density model. To account for possible uncertainties in the geological interpretation and for local heterogeneities that are not resolved by the surface map, we adopt conservative fluctuation ranges in both density and segment length. Specifically, we allow the density in each segment to vary independently within $\pm 10\%$ of its reference value, and the effective lengths of the segments to fluctuate within $\pm 10\%$ while keeping the total baseline length fixed, as detailed below.

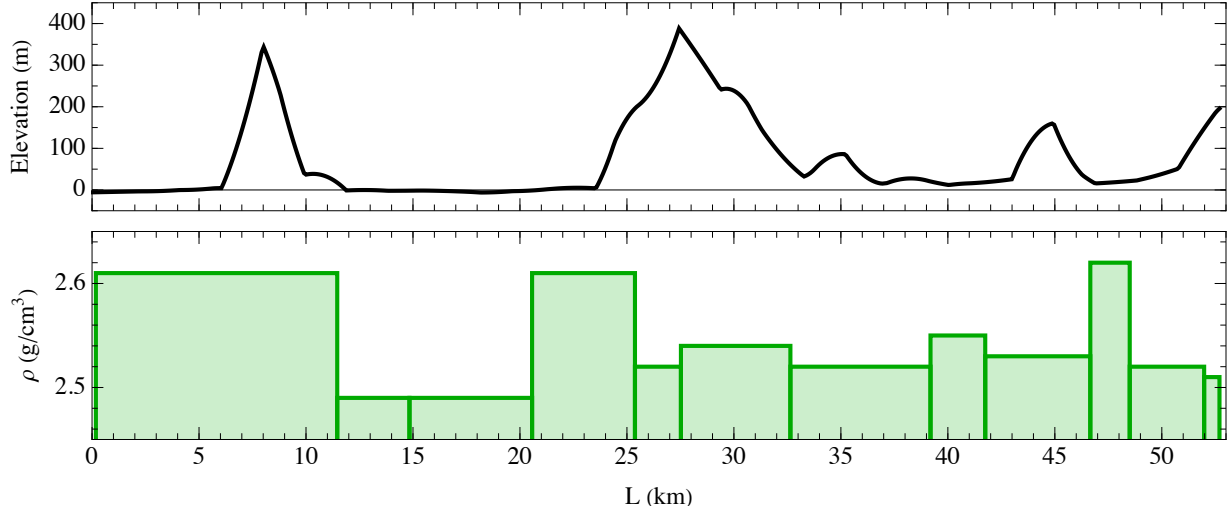


Figure 2: Geological sampling from Taishan to Jiangmen; the upper panel shows the surface elevation, and the lower panel shows the matter density of surface rocks along the TS–JUNO baseline.

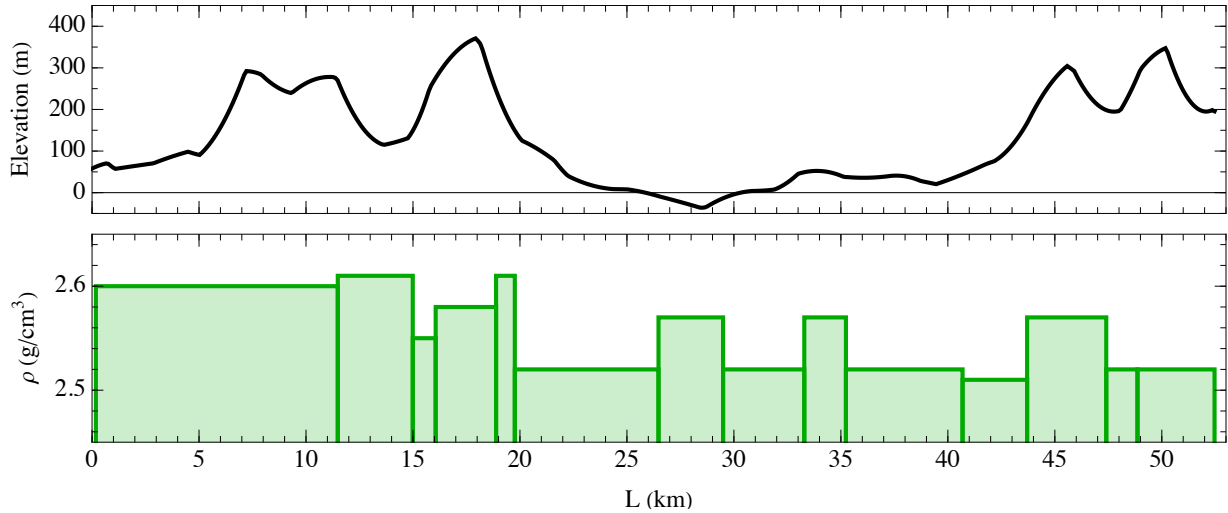


Figure 3: Geological sampling from Yangjiang to Jiangmen; the upper panel shows the surface elevation, and the lower panel shows the matter density of surface rocks along the YJ–JUNO baseline.

(i) Fluctuations of segment densities. To model the uncertainty of the crustal density itself, we allow each segment density to fluctuate around its reference value,

$$\rho_i = \rho_i^{(0)} (1 + \delta\rho_i), \quad |\delta\rho_i| \leq 10\%, \quad (2.4)$$

where $\delta\rho_i$ are treated as independent random variables uniformly distributed in the interval $[-0.1, 0.1]$.[¶] The total baseline length is kept fixed, $L_i = L_i^{(0)}$, in this case. For a given realization of $\{\delta\rho_i\}$ the

[¶]In the numerical analysis of Sec. 4 we include the density fluctuations only for the rock segments. The density of the air segment is kept fixed at $\rho = 0$, although its geometric length is allowed to fluctuate together with the other segments, see below.

corresponding average density reads

$$\rho_{\rho}^{\text{Average}} = \frac{1}{L} \sum_i \rho_i L_i^{(0)} = \rho^{\text{Average}} + \frac{1}{L} \sum_i \rho_i^{(0)} L_i^{(0)} \delta \rho_i, \quad (2.5)$$

so that the relative deviation from the reference value, $\Delta \rho_{\rho}^{\text{Average}} \equiv \rho_{\rho}^{\text{Average}} - \rho^{\text{Average}}$, is directly given by a weighted average of the segment fluctuations $\delta \rho_i$. In the numerical scan in Sec. 4 we find that for $|\delta \rho_i| \leq 10\%$ the typical (one-standard-deviation) fluctuation of ρ^{Average} is of order 1.5% for both baselines, and 95% of the random realizations lie within about $\pm 3\%$ around the reference value. Thus, even if each segment is allowed to vary independently within $\pm 10\%$, the baseline-averaged density remains remarkably stable at the percent level.

It is also instructive to consider the opposite limiting case in which the density fluctuations of all segments are fully correlated. In this case we may write

$$\delta \rho_i \equiv \delta, \quad |\delta| \leq 10\%, \quad (2.6)$$

so that all segment densities are rescaled by the same factor, $\rho_i = \rho_i^{(0)}(1 + \delta)$. The corresponding average density is then given by

$$\rho_{\text{corr}}^{\text{Average}} = \frac{1}{L} \sum_i \rho_i^{(0)}(1 + \delta) L_i^{(0)} = (1 + \delta) \rho^{\text{Average}}, \quad (2.7)$$

and the relative deviation of the average density is simply

$$\frac{\rho_{\text{corr}}^{\text{Average}} - \rho^{\text{Average}}}{\rho^{\text{Average}}} = \delta. \quad (2.8)$$

If the common fluctuation δ is assumed to be uniformly distributed in the interval $[-0.1, 0.1]$, the associated one-standard-deviation fluctuation is $\sigma_{\delta} = 0.1/\sqrt{3} \simeq 5.8\%$, and the full allowed range of ρ^{Average} extends up to $\pm 10\%$ around the reference value. This fully correlated scenario corresponds to a global mis-normalization of the crustal density scale, rather than to local heterogeneities between different segments. In the following we treat it as a conservative upper bound on possible shifts of the effective average density; its impact on the oscillation probabilities is effectively illustrated by the constant-density variations considered in Sec. 4.

(ii) Fluctuations of segment lengths. The uncertainties of the segment boundaries correspond to uncertainties in the segment lengths. A physically motivated way to describe them is to regard the internal interfaces along the baseline as being known only up to a finite longitudinal resolution. Denoting the original positions of the interfaces by $x_k^{(0)}$ ($k = 1, \dots, N + 1$), with $x_1^{(0)} = 0$, $x_{N+1}^{(0)} = L$ and $L_i^{(0)} = x_{i+1}^{(0)} - x_i^{(0)}$, we allow each internal point ($k = 2, \dots, N$) to move independently within a small interval around its reference position,

$$x_k = x_k^{(0)} + \Delta x_k, \quad -\alpha L_{k-1}^{(0)} \leq \Delta x_k \leq \alpha L_k^{(0)}, \quad (2.9)$$

where we take $\alpha = 0.1$ as a conservative estimate. The new segment lengths are then given by

$$L_i = x_{i+1} - x_i = L_i^{(0)} + \delta L_i, \quad \delta L_i \equiv \Delta x_{i+1} - \Delta x_i. \quad (2.10)$$

By construction the baseline length remains exactly fixed, $\sum_i L_i = x_{N+1} - x_1 = L$, and neighbouring segments are anti-correlated: if an interface moves to the right, the segment on its left becomes shorter and that on its right becomes longer. We stress that this picture corresponds closely to the physical origin of the geometric uncertainty, namely the limited knowledge of where exactly the geological interfaces intersect the oscillation baseline.

In this case we keep the segment densities fixed at their reference values, $\rho_i = \rho_i^{(0)}$, and the average density becomes

$$\rho_L^{\text{Average}} = \frac{1}{L} \sum_i \rho_i^{(0)} L_i = \rho^{\text{Average}} + \frac{1}{L} \sum_i (\rho_i^{(0)} - \rho^{\text{Average}}) \delta L_i. \quad (2.11)$$

Equation (2.11) makes it clear why the impact of the segment-length fluctuations on ρ^{Average} is much smaller than that of the density fluctuations in Eq. (2.5). Only the deviations of each segment density from the already narrow band around ρ^{Average} enter, and the contributions from the different segments tend to cancel because the δL_i are constrained by $\sum_i \delta L_i = 0$ and are strongly anti-correlated through Eq. (2.10). Numerically we find that for $|\delta L_i|/L_i^{(0)} \lesssim 10\%$ the typical fluctuation of ρ^{Average} induced by the length variations alone is only of order 10^{-3} , i.e. at the level of a few 0.01%, for both baselines. Therefore the geometrical uncertainty of the segment lengths has a negligible impact on the effective average matter density.||

(iii) Combined fluctuations of densities and lengths. Finally, in order to mimic a conservative and yet realistic matter profile uncertainty, we allow both the segment densities and the segment lengths to fluctuate simultaneously according to Eqs. (2.4), (2.9) and (2.10). To leading order in the small quantities $\delta\rho_i$ and δL_i , the deviation of the average density can be written as

$$\rho_{\rho+L}^{\text{Average}} \simeq \rho_\rho^{\text{Average}} + (\rho_L^{\text{Average}} - \rho^{\text{Average}}), \quad (2.12)$$

so that the variances of the two contributions approximately add. Since the length-induced part is suppressed by the small spread of the segment densities around ρ^{Average} and by cancellations between neighbouring segments, its variance is much smaller than that induced by the density fluctuations. Therefore the distribution of $\rho_{\rho+L}^{\text{Average}}$ is practically indistinguishable from that obtained in the density-only case in Eq. (2.5). In particular, the typical size of the fluctuation of the average density for $|\delta\rho_i| \leq 10\%$ remains at the level of $\mathcal{O}(1\%)$, while the additional uncertainty from the segment-length fluctuations stays at the $\mathcal{O}(10^{-3})$ level. As a consequence, in the discussion of matter effects on the reactor antineutrino oscillation probabilities in Sec. 4 we will focus on the impact of the density fluctuations, and treat the uncertainty due to the geometric segmentation as a subdominant effect.

|| As a cross-check we have also considered a simpler scheme in which each segment length is independently rescaled according to $L_i \rightarrow L_i^{(0)}(1 + \delta L_i)$ with $|\delta L_i| \leq 10\%$, followed by a global rescaling of all L_i such that the total baseline length L is restored. This alternative model slightly overestimates the effect of length fluctuations, but still yields fluctuations of ρ^{Average} at the level of $\sim 0.05\%$, fully consistent with the more realistic interface-displacement model described by Eqs. (2.9) and (2.10).

3 Neutrino oscillations in matter

In this section, we recap the fundamental formulas for three-flavor neutrino oscillations in matter and introduce an efficient semi-analytical method for exact calculations.

In vacuum, the neutrino oscillations are governed by a Schrödinger-like evolution equation in the flavor basis,

$$i \frac{d}{dx} \nu_\alpha(x) = H_{\text{vac}} \nu_\alpha(x), \quad (3.1)$$

where $\nu_\alpha = (\nu_e, \nu_\mu, \nu_\tau)^T$ denotes the flavor eigenstate vector and x the distance neutrinos have travelled. The vacuum Hamiltonian reads

$$H_{\text{vac}} = \frac{1}{2E_\nu} \left[U \begin{pmatrix} 0 & 0 & 0 \\ 0 & \Delta m_{21}^2 & 0 \\ 0 & 0 & \Delta m_{31}^2 \end{pmatrix} U^\dagger \right], \quad (3.2)$$

where E_ν is the neutrino energy.

For reactor antineutrino experiments, we are interested in the survival probability of electron antineutrinos, $P(\bar{\nu}_e \rightarrow \bar{\nu}_e)$, which can be written in a compact form as [20, 28]:

$$\begin{aligned} P(\bar{\nu}_e \rightarrow \bar{\nu}_e) = & 1 - \sin^2 2\theta_{12} \cos^4 \theta_{13} \sin^2 \frac{\Delta m_{21}^2 L}{4E_\nu} \\ & - \frac{1}{2} \sin^2 2\theta_{13} \left(\sin^2 \frac{\Delta m_{31}^2 L}{4E_\nu} + \sin^2 \frac{\Delta m_{32}^2 L}{4E_\nu} \right) \\ & - \frac{1}{2} \cos 2\theta_{12} \sin^2 2\theta_{13} \sin \frac{\Delta m_{21}^2 L}{4E_\nu} \sin \frac{(\Delta m_{31}^2 + \Delta m_{32}^2)L}{4E_\nu}, \end{aligned} \quad (3.3)$$

where L denotes the baseline length.

When neutrinos propagate in matter, coherent forward scattering on electrons induces an effective potential [23, 24] that modifies the Hamiltonian. Therefore, the effective Hamiltonian of antineutrinos in the flavor basis reads

$$H(x) = \frac{1}{2E_\nu} \left[U \begin{pmatrix} 0 & 0 & 0 \\ 0 & \Delta m_{21}^2 & 0 \\ 0 & 0 & \Delta m_{31}^2 \end{pmatrix} U^\dagger - \begin{pmatrix} A(x) & 0 & 0 \\ 0 & 0 & 0 \\ 0 & 0 & 0 \end{pmatrix} \right], \quad (3.4)$$

with

$$A(x) = 2\sqrt{2} G_F N_e(x) E_\nu \simeq 1.52 \times 10^{-7} \text{ eV}^2 \times Y_e \left[\frac{\rho(x)}{\text{g} \cdot \text{cm}^{-3}} \right] \times \left[\frac{E_\nu}{\text{MeV}} \right]. \quad (3.5)$$

Here G_F is the Fermi constant, $N_e(x)$ the electron number density, $\rho(x)$ the matter density, and Y_e the electron fraction per nucleon, which is typically $Y_e \simeq 0.5$ in the crust of the Earth.

Under the approximation of a constant matter density along the baseline, we have $\rho(x) \simeq \bar{\rho}$ and $A(x) \simeq \bar{A} = 2\sqrt{2} G_F \bar{N}_e E_\nu$, which leads to an x -independent Hamiltonian H^C of Eq. 3.4. The evolution operator over a baseline L then takes the simple form $S^C(L) = \exp[-i H^C L]$, and the corresponding $\bar{\nu}_e$ survival probability can be calculated as $P_{ee}^C(E_\nu, L) = |S_{ee}^C(L)|^2$.

Approximate analytic expressions for P_{ee}^C in the three-flavor neutrino oscillation framework, valid for reactor experiments, can be found in Ref. [25], where the leading matter corrections were shown to be relevant for precision measurements of Δm_{21}^2 and $\sin^2 \theta_{12}$ and mass ordering. The exact three-flavor oscillation probabilities in constant-density matter for arbitrary flavor transitions can be written in fully analytical form, see for example Refs. [29–37], while a variety of compact approximate formulas tailored to different experimental regimes are available in Refs. [25, 38–45].

In a realistic and accurate manner, the crust consists of different geological units with different densities, and the baselines from each reactor complex to the detector cross multiple rock formations. To take this into account, we consider a position-dependent matter density profile $\rho(x)$ obtained from local geological surveys and geophysical data. For practical calculations, it is convenient to approximate $\rho(x)$ by a set of N segments with piecewise constant densities,

$$\rho(x) \simeq \rho_i, \quad x_{i-1} < x < x_i, \quad i = 1, \dots, N, \quad (3.6)$$

with segment lengths $L_i = x_i - x_{i-1}$ satisfying $\sum_{i=1}^N L_i = L$.

In each segment the Hamiltonian H_i is constant, so the evolution operator in the corresponding segment is

$$S_i = \exp[-i H_i L_i] = \exp[-i M_i L_i / (2E_\nu)], \quad (3.7)$$

where M_i is the effective mass-squared matrix in matter. According to the Cayley–Hamilton theorem, the matrix exponential S_i for a 3×3 matrix can be expressed as a quadratic polynomial in M_i [34, 46, 47],

$$S_i = s_0 I + s_1 M_i + s_2 M_i^2, \quad (3.8)$$

where I is the 3×3 identity matrix, and the coefficients s_k ($k = 0, 1, 2$) are determined by the eigenvalues λ_k of M_i (or equivalently of $M'_i = U^\dagger M_i U$). Explicitly one has

$$\begin{aligned} s_0 &= -\frac{\lambda_1 \lambda_2 e^{-i \lambda_3 L_i / (2E_\nu)}}{(\lambda_2 - \lambda_3)(\lambda_3 - \lambda_1)} - \frac{\lambda_2 \lambda_3 e^{-i \lambda_1 L_i / (2E_\nu)}}{(\lambda_1 - \lambda_2)(\lambda_3 - \lambda_1)} - \frac{\lambda_1 \lambda_3 e^{-i \lambda_2 L_i / (2E_\nu)}}{(\lambda_1 - \lambda_2)(\lambda_2 - \lambda_3)}, \\ s_1 &= +\frac{(\lambda_1 + \lambda_2)e^{-i \lambda_3 L_i / (2E_\nu)}}{(\lambda_2 - \lambda_3)(\lambda_3 - \lambda_1)} + \frac{(\lambda_2 + \lambda_3)e^{-i \lambda_1 L_i / (2E_\nu)}}{(\lambda_1 - \lambda_2)(\lambda_3 - \lambda_1)} + \frac{(\lambda_1 + \lambda_3)e^{-i \lambda_2 L_i / (2E_\nu)}}{(\lambda_1 - \lambda_2)(\lambda_2 - \lambda_3)}, \\ s_2 &= -\frac{e^{-i \lambda_3 L_i / (2E_\nu)}}{(\lambda_2 - \lambda_3)(\lambda_3 - \lambda_1)} - \frac{e^{-i \lambda_1 L_i / (2E_\nu)}}{(\lambda_1 - \lambda_2)(\lambda_3 - \lambda_1)} - \frac{e^{-i \lambda_2 L_i / (2E_\nu)}}{(\lambda_1 - \lambda_2)(\lambda_2 - \lambda_3)}. \end{aligned} \quad (3.9)$$

The eigenvalues λ_k ($k = 1, 2, 3$) can be written in analytic form [29, 30, 33] as

$$\begin{aligned} \lambda_1 &= \frac{1}{3}x - \frac{1}{3}\sqrt{x^2 - 3y} \left[z + \sqrt{3(1 - z^2)} \right], \\ \lambda_2 &= \frac{1}{3}x + \frac{1}{3}\sqrt{x^2 - 3y} \left[z - \sqrt{3(1 - z^2)} \right], \\ \lambda_3 &= \frac{1}{3}x + \frac{2}{3}z\sqrt{x^2 - 3y}. \end{aligned} \quad (3.10)$$

where

$$x = \Delta m_{21}^2 + \Delta m_{31}^2 - A,$$

$$y = \Delta m_{21}^2 \Delta m_{31}^2 - A [\Delta m_{21}^2 (1 - \sin^2 \theta_{12} \cos^2 \theta_{13}) + \Delta m_{31}^2 (1 - \sin^2 \theta_{13})],$$

$$z = \cos \left[\frac{1}{3} \arccos \frac{2x^3 - 9xy - 27A\Delta m_{21}^2 \Delta m_{31}^2 \cos^2 \theta_{12} \cos^2 \theta_{13}}{2(x^2 - 3y)^{3/2}} \right]. \quad (3.11)$$

The full evolution operator for a baseline L is obtained by multiplying the segment operators in the propagation order

$$S^{\text{Vari}}(L) = S_N S_{N-1} \cdots S_1, \quad (3.12)$$

where the superscript “Vari” refers to the variable density profile. The corresponding survival probability is

$$P_{ee}^{\text{Vari}}(E_\nu, L) = |S_{ee}^{\text{Vari}}(L)|^2. \quad (3.13)$$

Note that an arbitrary matter-density profile $\rho(x)$ can be approximated with controllable accuracy by choosing a sufficiently large number of segments N , so that this semi-analytical treatment allows one to achieve the desired precision for realistic, position-dependent density profiles. This semi-analytical approach, in which the realistic crustal profile is represented by a finite number of constant-density segments, provides an accurate and efficient way to calculate the oscillation probabilities of neutrinos in a non-uniform medium. Note that this framework has been written for antineutrinos, and the corresponding expressions for neutrinos can be obtained by changing $U \rightarrow U^*$ and $A \rightarrow -A$ in the effective Hamiltonian of Eq. (3.4).

4 Numerical results

In this section we present our numerical results for the matter effects on the $\bar{\nu}_e \rightarrow \bar{\nu}_e$ survival probability along the TS–JUNO and YJ–JUNO baselines. We first quantify the impact of variable matter density on the oscillation probability, and then discuss its implications for the precision measurement of oscillation parameters and for the determination of the neutrino mass ordering.

To start, we shall employ the current global best-fit values of the three-flavor oscillation parameters, based on the NuFIT 6.0 (2024) analysis [5]. For the JUNO baselines, we consider the locations of the JUNO site as well as the YJ and TS nuclear power plants [16]. The TS–JUNO and YJ–JUNO baselines are determined based on the average positions of the individual reactor cores. For the Taishan complex, we use $L_{\text{TS}} = 52.695$ km, which represents the average distance from the first and second cores to JUNO. For the Yangjiang complex, we adopt $L_{\text{YJ}} = 52.465$ km, corresponding to the average distance from the third and fourth cores to JUNO.

The matter density along each baseline is described by the segmented piecewise-constant profiles constructed in Sec. 2, specifically utilizing the sets $\{\rho_i^{(0)}, L_i^{(0)}\}$ introduced in Sec. 2.1 and Sec. 2.2, including the initial air segment where $\rho = 0$. The corresponding baseline-averaged densities are defined in Eq. (2.11). Using the segment information presented in Tables 1 and 2, we find

$$\rho_{\text{TS}}^{\text{Average}} \simeq 2.541 \text{ g/cm}^3, \quad (4.14)$$

and

$$\rho_{\text{YJ}}^{\text{Average}} \simeq 2.554 \text{ g/cm}^3, \quad (4.15)$$

which will serve as benchmark constant densities for the subsequent analysis. We also specified conservative fluctuation ranges of $\pm 10\%$ for both the segment densities and segment lengths as discussed in Sec. 2.2.

First, we examine the absolute magnitude of variable matter effects on the $\bar{\nu}_e \rightarrow \bar{\nu}_e$ survival probability. As shown in Fig. 4, the absolute differences between vacuum survival probability P_{ee}^{Vac} and variable-matter survival probability P_{ee}^{Vari} are presented for the reference matter density profiles along the TS–JUNO and YJ–JUNO baselines. One can observe that they are at the percent level and will be comparable to the expected uncertainties of Δm_{21}^2 and $\sin^2 \theta_{12}$. This conclusion is rather consistent with Ref. [25] using the constant density approximation.

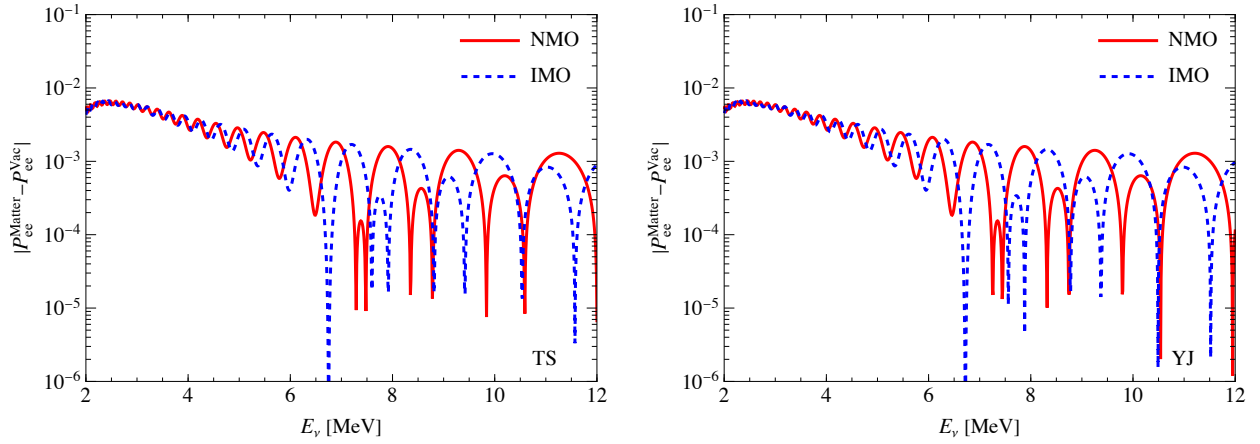


Figure 4: The absolute differences between P_{ee} in matter and in vacuum using the reference matter density profiles.

Next we will discuss the effects of variable density profiles. Considering the potential correlations in the density fluctuations of connected or nearby segments, we analyze two extreme scenarios:

- Scenario A: profiles in which the densities of all rock segments are coherently rescaled within a permitted $\pm 10\%$, corresponding to global upward or downward shifts of the baseline-averaged density;
- Scenario B: profiles in which the densities of all rock segments are randomly rescaled within the allowed $\pm 10\%$ band, thus fine structures of the density variations are allowed.

All these sampled representative profiles satisfy $|\delta \rho_i| \leq 10\%$ and $|\delta L_i|/L_i^{(0)} \leq 10\%$ for every segment, and their baseline-averaged densities lie within the $\sim 1\text{--}3\%$ band around the reference values quantified in Sec. 2.2.

Using the benchmark constant density profiles in Eqs. (4.14) and Eq. (4.15), we compare the effects of variable matter against the corresponding constant approximation in Fig. 5 for both the TS–JUNO

and YJ-JUNO baselines. In each panel, the black and gray curves represent Scenario A, where the constant reference density is coherently increased or decreased within a 10% range, respectively. These curves serve as a simple benchmark for the effect of fully correlated uncertainty in the reference crustal density profile, which is on the order of 10^{-3} , in contrast to the total contributions at the percent level. In contrast, the colored curves illustrate five representative realizations of fluctuations in Scenario B, generated by allowing the density in each rock segment along the baseline to vary independently within the 10% range. It is important to note that the differences in survival probability are significantly smaller in Scenario B than in Scenario A due to the effects of statistical averaging.

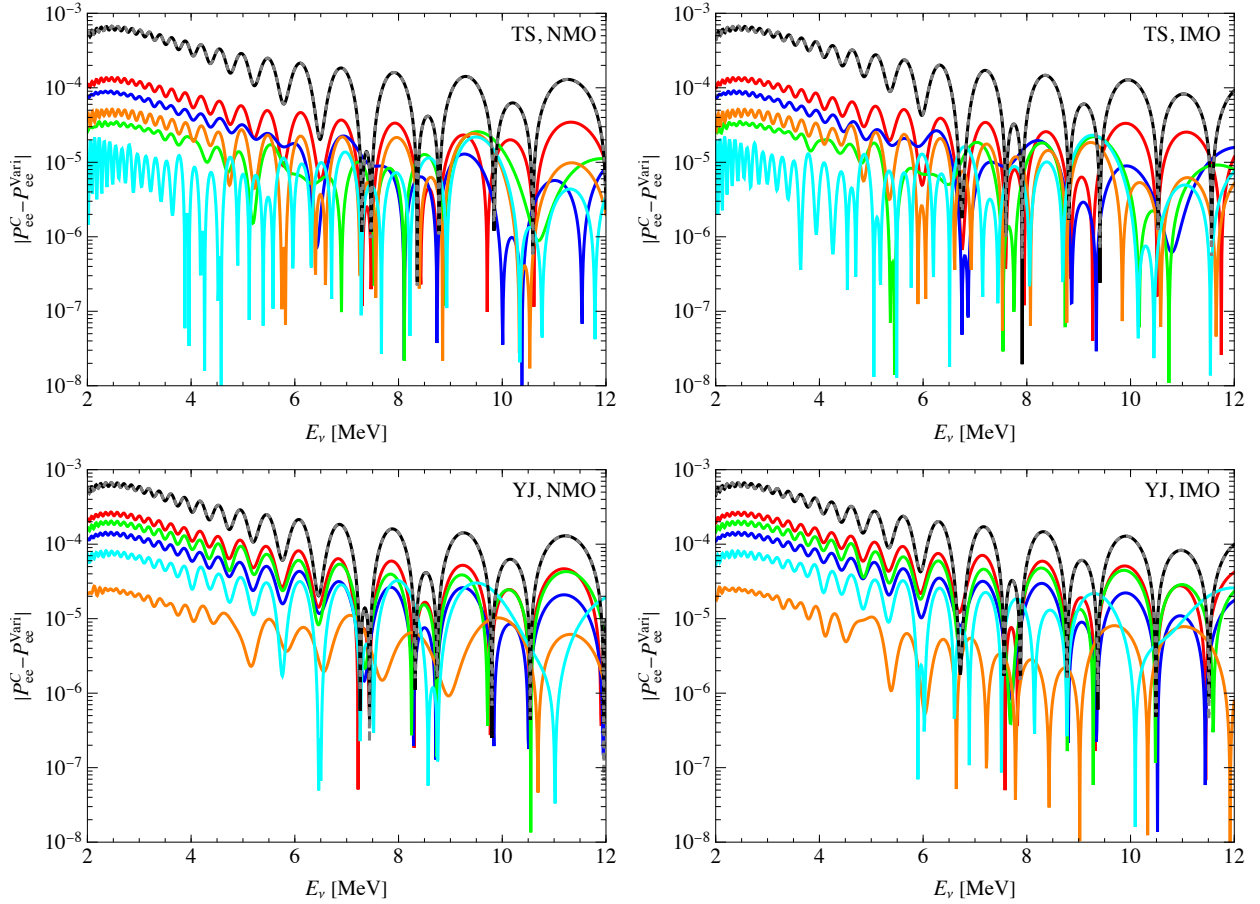


Figure 5: Variable matter effects on the $\bar{\nu}_e \rightarrow \bar{\nu}_e$ survival probability along the TS-JUNO (upper panel) and YJ-JUNO (lower panel) baselines for NMO (left panel) and IMO (right panel).

Now we discuss how the variable matter effects affects the measurement of oscillation parameters and mass ordering. From the first reactor antineutrino oscillation result of JUNO [21], the precision of Δm_{21}^2 and $\sin^2 \theta_{12}$ reached 1.55% and 2.81% respectively. Meanwhile, it will reach to 0.3% and 0.5% in 6 yrs and even smaller for the entire lifetime of 20 yrs.

In Fig. 6, the comparison of the survival probability differences between the oscillation parameter variation and the density profile variation is illustrated. As an illustration, Fig. 6 shows the absolute differences in the survival probability, $|P_{ee}^X - P_{ee}^{\text{BF}}|$ for the TS-JUNO baseline and NMO, where P_{ee}^{BF}

is the probability calculated with the best-fit values, and P_{ee}^X with one of the parameters shifted according to the expected JUNO precision. For clarity, in each panel only one parameter is varied at a time, while the others are fixed at their best-fit values. The black and grey lines are that of variable density profile with the uncertainty of Scenario A. From the figures, one can read that the uncertainty of matter density profiles is more than one order of magnitude smaller than the current precision of oscillation parameters, but will increase to 20% or 50% for longer running time. Therefore a careful investigation and modelling of the density profiles is needed in the future.

We now turn to the impact of variable matter density profiles on mass ordering determination. In the upper panels of Fig. 7, we illustrate the differences in survival probabilities between NMO and IMO as follows:

$$P_{ee}^{\text{C,MO}}(E_\nu) = |P_{ee}^{\text{C,NMO}}(E_\nu) - P_{ee}^{\text{C,IMO}}(E_\nu)|, \quad (4.16)$$

for the constant density profiles. Similarly, we can define the differences in survival probabilities for variable density profiles as:

$$P_{ee}^{\text{Vari,MO}}(E_\nu) = |P_{ee}^{\text{Vari,NMO}}(E_\nu) - P_{ee}^{\text{Vari,IMO}}(E_\nu)|, \quad (4.17)$$

and illustrate the absolute differences of these quantities in the lower panels of Fig. 7. Note that the black and gray curves represent Scenario A, while the colored curves correspond to Scenario B. By comparing the magnitudes of these differences, we conclude that variations in matter density profiles contribute only 1% to the mass ordering sensitivity, making them relatively negligible. Therefore, we can assert that the additional uncertainty introduced by the imperfect knowledge of the matter density profile is insignificant, and the determination of mass ordering remains robust against realistic variable matter density effects.

5 Impact of anomalous density perturbations

In previous discussions, we have assumed that the matter density along the TS-JUNO and YJ-JUNO baselines can be described by a piecewise-constant profile with moderate segmented fluctuations, typically on the order of $\pm 10\%$ around the reference rock densities. This approach is well justified by the geological information available along the JUNO baselines.

In this section, however, we will explore the possibility of shallow crust tomography using reactor antineutrinos, considering the potential existence of localized structures that may deviate more significantly from the average crustal rock. These structures could include water-filled regions, underground reservoirs, or localized low-density cavities within fractured rocks.

For definiteness, let us consider a single localized anomaly with length ΔL_a and density ρ_a embedded in an otherwise standard rock profile characterized by an average density $\bar{\rho}_0$. If the baseline length is L , the new baseline-averaged density becomes

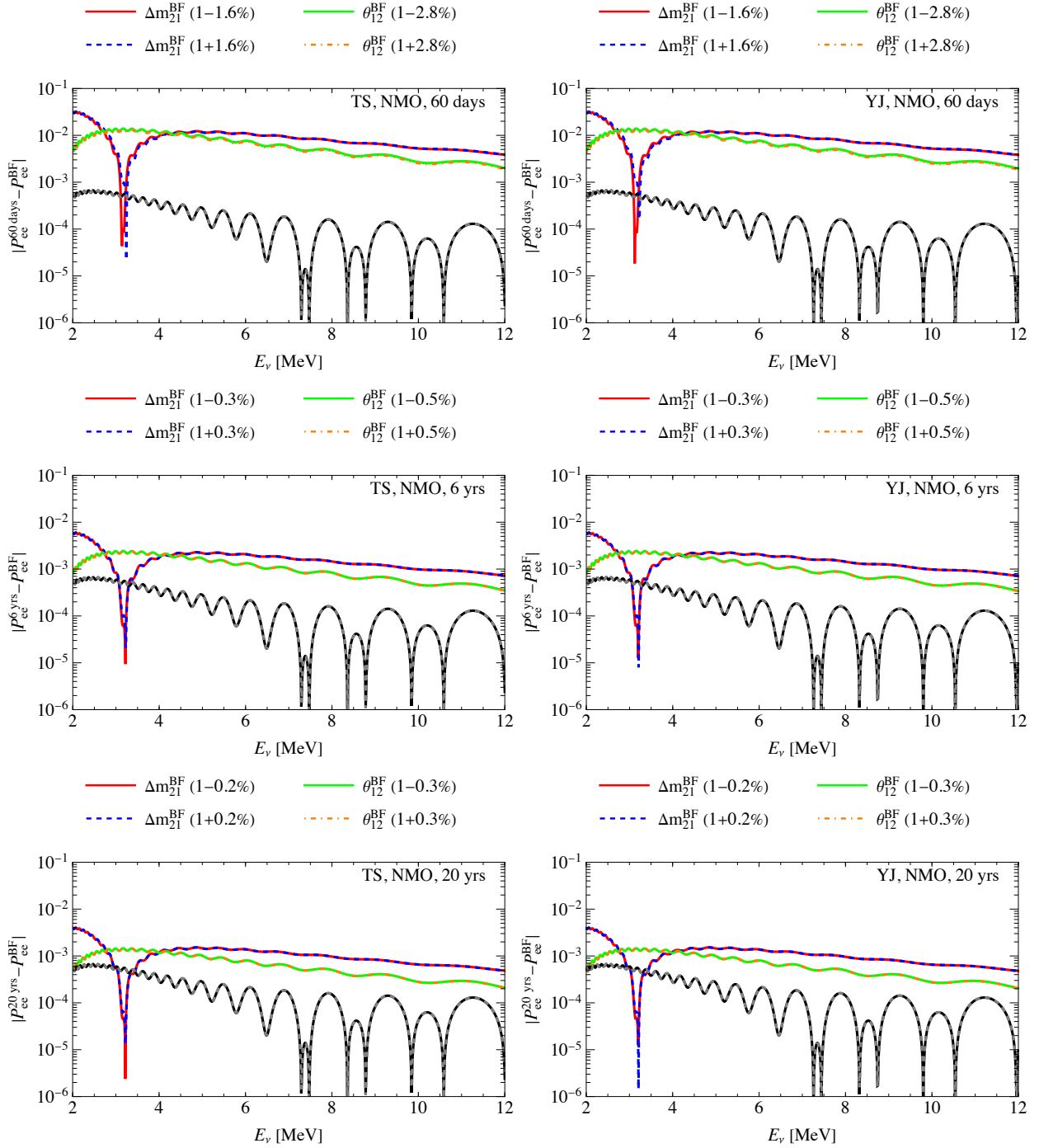


Figure 6: Impact of the uncertainties of Δm_{21}^2 , and θ_{12} on the $\bar{\nu}_e \rightarrow \bar{\nu}_e$ survival probability along the TS–JUNO (YJ–JUNO) baseline for normal mass ordering. The three panels in each column correspond to parameter uncertainties after 60 days, 6 years (6 yrs), 20 years (20 yrs) of data taking. In each panel, only one parameter is varied at a time, while the others are fixed to their best-fit values. And the black/gray lines denote 10% variation of the benchmark constant density, namely, $\rho_{\text{TS}}^{\text{Average}}$ and $\rho_{\text{YJ}}^{\text{Average}}$ as shown in Figure 5.

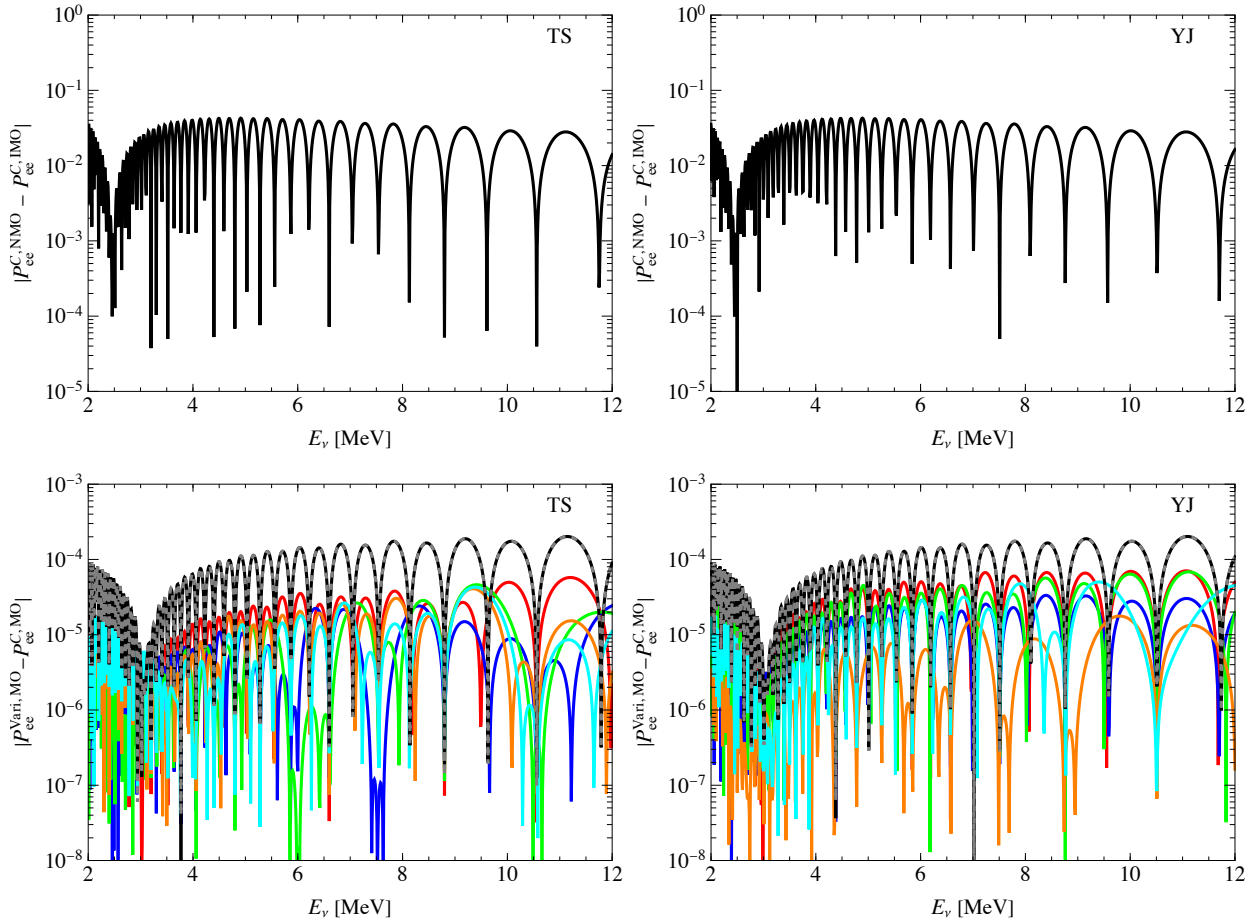


Figure 7: Variable matter effects on the mass-ordering determination. Top row: absolute difference $|P_{ee}^{C,MO} - P_{ee}^{C,IMO}|$ between the constant-density survival probabilities in NMO and IMO for the TS–JUNO (left) and YJ–JUNO (right) baselines. Middle row: deviation $|P_{ee}^{Vari,MO} - P_{ee}^{C,MO}|$ induced by density fluctuations. Bottom row: relative deviation $|P_{ee}^{Vari,MO} - P_{ee}^{C,MO}|/P_{ee}^{C,MO}$.

$$\bar{\rho}' = \frac{1}{L} [\rho_a \Delta L_a + \bar{\rho}_0 (L - \Delta L_a)] = \bar{\rho}_0 + \delta \bar{\rho}, \quad (5.18)$$

with the relative shift of

$$\frac{\delta \bar{\rho}}{\bar{\rho}_0} = \left(\frac{\rho_a}{\bar{\rho}_0} - 1 \right) \frac{\Delta L_a}{L}. \quad (5.19)$$

This straightforward expression indicates that, even if ρ_a differs significantly from the typical rock density, its impact on the baseline-averaged density is suppressed by the ratio $\Delta L_a/L$. To quantify this effect, we take $\bar{\rho}_0 \simeq 2.6 \text{ g/cm}^3$ as a representative crustal density and $L \simeq 53 \text{ km}$ as a typical baseline. A water-like anomaly corresponds roughly to $\rho_a \simeq 1.0 \text{ g/cm}^3$, while an air-filled cavity has $\rho_a \simeq 0$ on the scale relevant for matter effects. For a 1 km-long water anomaly one finds

$$\frac{\delta \bar{\rho}}{\bar{\rho}_0} \simeq \left(\frac{1.0}{2.6} - 1 \right) \frac{1 \text{ km}}{53 \text{ km}} \approx -1.2\%, \quad (5.20)$$

and for an air cavity of the same length,

$$\frac{\delta\bar{\rho}}{\bar{\rho}_0} \simeq (0 - 1) \frac{1 \text{ km}}{53 \text{ km}} \approx -1.9\%. \quad (5.21)$$

Shorter or more localized structures (e.g., $\Delta L_a \lesssim 0.5 \text{ km}$) lead to relative shifts of $\lesssim 1\%$, while more extended anomalous regions are disfavored by the available geological information along the baselines.

The matter potential in the flavor basis is proportional to the electron number density,

$$A = 2\sqrt{2} G_F N_e E_\nu \propto \rho, \quad (5.22)$$

so that the fractional change of the effective potential is $\delta A/A \simeq \delta\bar{\rho}/\bar{\rho}_0$. At the JUNO or future reactor antineutrino experiments, the standard matter effect induces only a percent-level modification of the $\bar{\nu}_e$ survival probability with respect to vacuum oscillations. Therefore, an additional $\mathcal{O}(1\%)$ change in the average density from a localized water-like or air-like anomaly leads to a further suppression of the matter effect by a few $\times 10^{-4}$ in the survival probability.

To make this conclusion more explicit, Fig. 8 illustrates, for the TS–JUNO baseline and NMO, the absolute difference of $|P_{ee}^{\text{Anomaly}} - P_{ee}^{\text{C}}|$ obtained in a constant-density profile and in profiles containing a localized air-like segment. The constant reference probability P_{ee}^{C} is computed assuming a uniform density $\rho_{\text{TS}}^{\text{Average}}$, and in the anomalous cases we keep the same uniform density $\rho_{\text{TS}}^{\text{Average}}$ along the whole baseline, except for an additional 1 km air layer (with $\rho \simeq 0$) inserted either at the beginning of the baseline (red curve, between 0 and 1 km), in the middle (blue curve, around $L/2$), or close to the detector (green curve, near the end of the baseline). Over the full neutrino energy window ($E_\nu \simeq 2\text{--}12 \text{ MeV}$), the induced differences remain at the level of a few $\times 10^{-4}$, in excellent agreement with the analytical estimate based on Eqs. (5.19)–(5.21). We have also verified that analogous configurations for the YJ–JUNO baseline and for IMO lead to very similar corrections. In addition replacing the anomalous air layer by a water-like segment with $\rho_a \simeq 1.0 \text{ g/cm}^3$ yields very similar results.

More generally, we have explicitly examined several extreme configurations in which a rock segment in the baseline model is replaced by either water or air, with ΔL_a extending up to the kilometer scale and located at various positions along the baseline. In all these cases, the resulting changes in $P(\bar{\nu}_e \rightarrow \bar{\nu}_e)$ were found to be much smaller than the effects of the typical $\pm 10\%$ segment-wise fluctuations discussed in Sec. 4. Therefore, we conclude that potential anomalous density structures, such as localized water-filled regions or air cavities, do not undermine the robustness of our conclusions regarding matter effects on reactor antineutrino oscillations at JUNO. As a result, an even larger detector is necessary for effective shallow crust tomography using reactor antineutrinos.

6 Summary

In this work, we have investigated the impact of realistic matter density variations on reactor antineutrino oscillations. Using geological information along the baselines from reactor nuclear power plants to the experimental hall, we constructed a piecewise-constant density model that approximates the

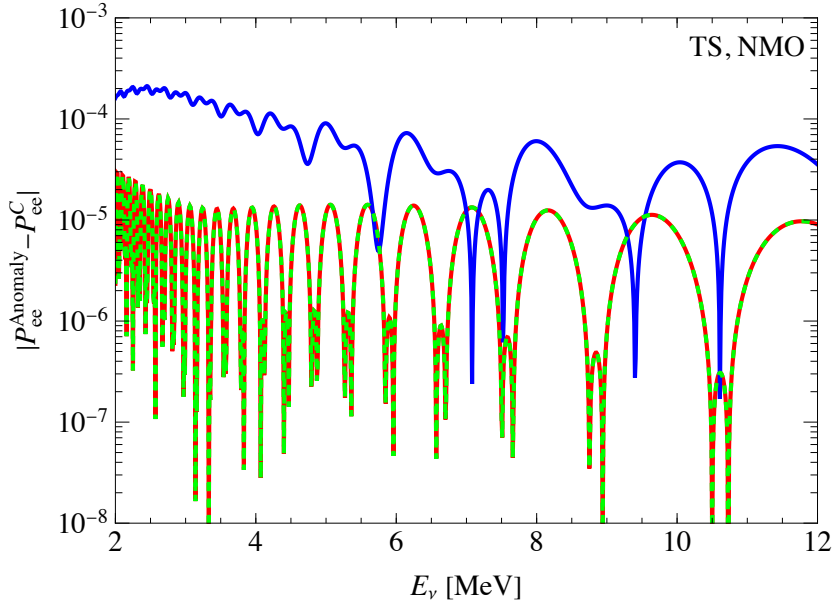


Figure 8: Absolute difference $|P_{ee}^{\text{Anomaly}} - P_{ee}^C|$ as a function of antineutrino energy E_{ν} for the TS–JUNO baseline in NMO. The constant-density reference probability P_{ee}^C is computed for a uniform matter density $\rho_{\text{TS}}^{\text{Average}}$, equal to the baseline-averaged density defined in Eqs. (4.14) and (4.15). The three colored curves correspond to profiles in which an additional 1 km air segment ($\rho \simeq 0$) is inserted at the beginning (red), in the middle (blue), or at the end (green) of the baseline, while the remaining path is kept at density $\rho_{\text{TS}}^{\text{Average}}$. The differences stay at the level of a few $\times 10^{-4}$ or smaller over the entire JUNO energy range, illustrating the negligible impact of such localized low-density anomalies on the reactor antineutrino survival probability.

South China crustal structure. We then allowed for conservative fluctuations of $\pm 10\%$ in the density of each segment and $\pm 10\%$ in the segment lengths, while keeping the total baseline lengths fixed. The resulting average matter densities and the conservative uncertainties are given as

$$\rho_{\text{TS}}^{\text{Average}} \simeq (2.541 \pm 10\%) \text{ g/cm}^3,$$

and

$$\rho_{\text{YJ}}^{\text{Average}} \simeq (2.554 \pm 10\%) \text{ g/cm}^3.$$

Within the standard three-flavor oscillation framework, we computed the $\bar{\nu}_e \rightarrow \bar{\nu}_e$ survival probabilities for both constant-density and variable-density profiles, and quantified the resulting differences for both normal and inverted mass orderings. We further assessed the implications of these differences on the precision measurement of the oscillation parameters Δm_{21}^2 and $\sin^2 \theta_{12}$ and neutrino mass ordering.

Our main conclusions can be summarized as follows:

- The absolute difference $|P_{ee}^C - P_{ee}^{\text{Vari}}|$ induced by realistic density variations is approximately 10^{-3} for the correlated density fluctuations of Scenario A, accounting for about 10% of the total

matter effects. While this effect is negligible at the current precision, it should be considered and addressed for future measurements aiming at millesimal precision.

- The mass-ordering discriminant $P_{ee}^{\text{C,MO}} = |P_{ee}^{\text{C,NMO}} - P_{ee}^{\text{C,IMO}}|$ is typically on the order of 10^{-3} – 10^{-2} , whereas the correction $|P_{ee}^{\text{Vari,MO}} - P_{ee}^{\text{C,MO}}|$ resulting from variable matter density is at most on the order of 10^{-4} . Consequently, realistic density variations may statistically alter the ordering discriminant by at most a few percent, which is negligible. Thus, the mass-ordering determination at JUNO is largely insensitive to the detailed structure of the crustal density along the baselines.

From a broader perspective, the commencement of JUNO’s data collection and the release of the first reactor antineutrino oscillation results signify an important advancement in the global neutrino program. Alongside Hyper-Kamiokande and DUNE, JUNO will contribute to completing the understanding of three-flavor oscillations by determining the mass ordering and significantly enhancing the precision of the mixing angles and mass-squared differences. With the advent of the era of precision measurements in neutrino physics, the contributions of sub-leading and subtle effects may need to be reconsidered, such as the variable matter density profile considered in this work. Other such efforts include studies of indirect unitarity violation effects [48], radiative corrections to neutrino propagation in matter and to elastic neutrino-electron scattering [49–51]. Systematically incorporating these effects will further increase the reliability of oscillation experiments, enhance their discovery potential [52], and support precise measurements of neutrino oscillation parameters and searches for related new physics.

Acknowledgments

Jing-yu Zhu thanks Wen-jie Wu for helpful discussions. The work of JYZ was supported in part by the National Key Research and Development Program of China (under grant number 2021YFA1601300) and by the National Natural Science Foundation of China (under grant number 12505134). The work of YFL was supported in part by the National Natural Science Foundation of China (under grant numbers 12075255). The work of ADW was supported in part by the Open Project Program of National Key Laboratory of Uranium Resources Exploration-Mining and Nuclear Remote Sensing (under grant number NKLUR-2024-QN-005). The work of YX was supported in part by the National Natural Science Foundation of China (under grant number 42074092).

References

[1] T. Kajita, *Nobel Lecture: Discovery of atmospheric neutrino oscillations*, *Rev. Mod. Phys.* **88** (2016), no. 3 030501.

[2] A. B. McDonald, *Nobel Lecture: The Sudbury Neutrino Observatory: Observation of flavor change for solar neutrinos*, *Rev. Mod. Phys.* **88** (2016), no. 3 030502.

[3] **Particle Data Group**, S. Navas et al., *Review of particle physics*, *Phys. Rev. D* **110** (2024), no. 3 030001.

[4] F. Capozzi, W. Giarè, E. Lisi, A. Marrone, A. Melchiorri, et al., *Neutrino masses and mixing: Entering the era of subpercent precision*, *Phys. Rev. D* **111** (2025), no. 9 093006, [2503.07752].

[5] I. Esteban, M. C. Gonzalez-Garcia, M. Maltoni, I. Martinez-Soler, J. P. Pinheiro, et al., *NuFit-6.0: updated global analysis of three-flavor neutrino oscillations*, *JHEP* **12** (2024) 216, [2410.05380].

[6] P. F. de Salas, D. V. Forero, S. Gariazzo, P. Martínez-Miravé, O. Mena, et al., *2020 global reassessment of the neutrino oscillation picture*, *JHEP* **02** (2021) 071, [2006.11237].

[7] B. Pontecorvo, *Mesonium and Antimesonium*, *Sov. Phys. JETP* **6** (1958) 429–431.

[8] Z. Maki, M. Nakagawa, and S. Sakata, *Remarks on the unified model of elementary particles*, *Prog. Theor. Phys.* **28** (1962) 870–880.

[9] B. Pontecorvo, *Neutrino Experiments and the Problem of Conservation of Leptonic Charge*, *Sov. Phys. JETP* **26** (1968) 984–988.

[10] **KATRIN**, M. Aker et al., *Direct neutrino-mass measurement with sub-electronvolt sensitivity*, *Nature Phys.* **18** (2022), no. 2 160–166, [2105.08533].

[11] M. Agostini, G. Benato, J. A. Detwiler, J. Menéndez, and F. Vissani, *Toward the discovery of matter creation with neutrinoless $\beta\beta$ decay*, *Rev. Mod. Phys.* **95** (2023), no. 2 025002, [2202.01787].

[12] **KamLAND-Zen**, S. Abe et al., *Search for Majorana Neutrinos with the Complete KamLAND-Zen Dataset*, 2406.11438.

[13] **Planck**, N. Aghanim et al., *Planck 2018 results. VI. Cosmological parameters*, *Astron. Astrophys.* **641** (2020) A6, [1807.06209]. [Erratum: *Astron. Astrophys.* 652, C4 (2021)].

[14] **Hyper-Kamiokande proto-collaboration**, K. Abe et al., *Hyper-kamiokande design report*, *arXiv preprint* (2018) [1805.04163].

[15] **DUNE**, B. Abi et al., *Deep underground neutrino experiment (dune), far detector technical design report*, *J. Instrum.* **15** (2020) T08008, [2002.02967].

[16] **JUNO**, F. An et al., *Neutrino Physics with JUNO*, *J. Phys. G* **43** (2016), no. 3 030401, [1507.05613].

[17] **JUNO**, P. Abusleme et al., *Juno physics and detector*, *Prog. Part. Nucl. Phys.* **123** (2022) 103927, [2104.02565].

[18] Y.-F. Li, J. Cao, Y. Wang, and L. Zhan, *Unambiguous Determination of the Neutrino Mass Hierarchy Using Reactor Neutrinos*, *Phys. Rev. D* **88** (2013) 013008, [1303.6733].

[19] **JUNO**, A. Abusleme et al., *Potential to identify neutrino mass ordering with reactor antineutrinos at JUNO*, *Chin. Phys. C* **49** (2025), no. 3 033104, [2405.18008].

[20] **JUNO**, A. Abusleme et al., *Sub-percent precision measurement of neutrino oscillation parameters with JUNO*, *Chin. Phys. C* **46** (2022), no. 12 123001, [2204.13249].

[21] **JUNO**, A. Abusleme et al., *First measurement of reactor neutrino oscillations at JUNO*, 2511.14593.

[22] **JUNO**, A. Abusleme et al., *Initial performance results of the JUNO detector*, 2511.14590.

[23] L. Wolfenstein, *Neutrino Oscillations in Matter*, *Phys. Rev. D* **17** (1978) 2369–2374.

[24] S. P. Mikheev and A. Y. Smirnov, *Resonant amplification of neutrino oscillations in matter and solar neutrino spectroscopy*, *Nuovo Cim. C* **9** (1986) 17–26.

[25] Y.-F. Li, Y. Wang, and Z.-z. Xing, *Terrestrial matter effects on reactor antineutrino oscillations at JUNO or RENO-50: how small is small?*, *Chin. Phys. C* **40** (2016), no. 9 091001, [1605.00900].

[26] F. Capozzi, E. Lisi, and A. Marrone, *Neutrino mass hierarchy and electron neutrino oscillation parameters with one hundred thousand reactor events*, *Phys. Rev. D* **89** (2014), no. 1 013001, [1309.1638].

[27] J. Deng, H. Chen, et al., *Rock Physical Properties Characteristics of Typical Uranium Deposits in China*. Science Press, Beijing, China, 2019. (in Chinese), ISBN: 978-7-03-060301-2.

[28] Z.-Z. Xing, *Interference effects in reactor antineutrino oscillations*, 1808.02256.

[29] V. D. Barger, K. Whisnant, S. Pakvasa, and R. J. N. Phillips, *Matter Effects on Three-Neutrino Oscillations*, *Phys. Rev. D* **22** (1980) 2718.

[30] H. W. Zaglauer and K. H. Schwarzer, *The Mixing Angles in Matter for Three Generations of Neutrinos and the Msw Mechanism*, *Z. Phys. C* **40** (1988) 273.

[31] V. A. Naumov, *Three neutrino oscillations in matter, CP violation and topological phases*, *Int. J. Mod. Phys. D* **1** (1992) 379–399.

[32] S. Toshev, *On T violation in matter neutrino oscillations*, *Mod. Phys. Lett. A* **6** (1991) 455–460.

- [33] Z.-z. Xing, *New formulation of matter effects on neutrino mixing and CP violation*, *Phys. Lett. B* **487** (2000) 327–333, [[hep-ph/0002246](#)].
- [34] T. Ohlsson and H. Snellman, *Three flavor neutrino oscillations in matter*, *J. Math. Phys.* **41** (2000) 2768–2788, [[hep-ph/9910546](#)]. [Erratum: *J.Math.Phys.* 42, 2345 (2001)].
- [35] M. Freund, *Analytic approximations for three neutrino oscillation parameters and probabilities in matter*, *Phys. Rev. D* **64** (2001) 053003, [[hep-ph/0103300](#)].
- [36] H. Zhang and Z.-z. Xing, *Leptonic unitarity triangles in matter*, *Eur. Phys. J. C* **41** (2005) 143–152, [[hep-ph/0411183](#)].
- [37] Z.-z. Xing, S. Zhou, and Y.-L. Zhou, *Renormalization-Group Equations of Neutrino Masses and Flavor Mixing Parameters in Matter*, *JHEP* **05** (2018) 015, [[1802.00990](#)].
- [38] E. K. Akhmedov, R. Johansson, M. Lindner, T. Ohlsson, and T. Schwetz, *Series expansions for three flavor neutrino oscillation probabilities in matter*, *JHEP* **04** (2004) 078, [[hep-ph/0402175](#)].
- [39] Y.-F. Li and S. Luo, *Neutrino Oscillation Probabilities in Matter with Direct and Indirect Unitarity Violation in the Lepton Mixing Matrix*, *Phys. Rev. D* **93** (2016), no. 3 033008, [[1508.00052](#)].
- [40] Z.-z. Xing and J.-y. Zhu, *Analytical approximations for matter effects on CP violation in the accelerator-based neutrino oscillations with $E \lesssim 1$ GeV*, *JHEP* **07** (2016) 011, [[1603.02002](#)].
- [41] S. Luo, *Neutrino Oscillation in Dense Matter*, *Phys. Rev. D* **101** (2020), no. 3 033005, [[1911.06301](#)].
- [42] X. Wang and S. Zhou, *On the properties of the effective Jarlskog invariant for three-flavor neutrino oscillations in matter*, *Nucl. Phys. B* **950** (2020) 114867, [[1908.07304](#)].
- [43] X. Wang and S. Zhou, *Analytical solutions to renormalization-group equations of effective neutrino masses and mixing parameters in matter*, *JHEP* **05** (2019) 035, [[1901.10882](#)].
- [44] Z.-Z. Xing and J.-Y. Zhu, *Sum rules and asymptotic behaviors of neutrino mixing in dense matter*, *Nucl. Phys. B* **949** (2019) 114803, [[1905.08644](#)].
- [45] J.-y. Zhu, *Radiative corrections to the lepton flavor mixing in dense matter*, *JHEP* **05** (2020) 097, [[2002.12182](#)].
- [46] C. Moler and C. V. Loan, *Nineteen dubious ways to compute the exponential of a matrix*, *SIAM Review* **20** (1978) 801.
- [47] Y.-F. Li, J. Zhang, S. Zhou, and J.-y. Zhu, *Looking into Analytical Approximations for Three-flavor Neutrino Oscillation Probabilities in Matter*, *JHEP* **12** (2016) 109, [[1610.04133](#)].

[48] Y.-F. Li, Z.-z. Xing, and J.-y. Zhu, *Indirect unitarity violation entangled with matter effects in reactor antineutrino oscillations*, *Phys. Lett. B* **782** (2018) 578–588, [1802.04964].

[49] J. Huang, T. Ohlsson, S. Vihonen, and S. Zhou, *Effects of the matter potential at one-loop level on neutrino oscillations in long-baseline experiments*, *Phys. Rev. D* **111** (2025), no. 11 116024, [2504.15998].

[50] J. Huang, T. Ohlsson, S. Vihonen, and S. Zhou, *One-Loop Effects in the Neutrino Matter Potential and Implications for Non-Standard Interactions*, 2510.04841.

[51] J. Huang and S. Zhou, *Elastic neutrino-electron scattering at the one-loop level in the standard model*, *Phys. Rev. D* **111** (2025), no. 3 033005, [2412.17047].

[52] Y. Wang, Z.-z. Xing, and S. Zhou, *Towards a detection of reactor $\bar{\nu}_e \rightarrow \bar{\nu}_\mu$ and $\bar{\nu}_e \rightarrow \bar{\nu}_\tau$ oscillations with possible CP violation*, 2509.00422.